

Supporting Information –

**Enhancing Ionic Conductivity in $\text{Li}_{6+x}\text{Ge}_x\text{P}_{1-x}\text{S}_5\text{Br}$: Impact of Li^+
Substructure on Ionic Transport and Solid-State Battery Performance**

Vasiliki Faka^a, Bibek Samanta^{b,c}, Martin A. Lange^{a,d}, Bianca Helm^e, Xabier Martinez de Irujo Labalde^a, Niklas Kierdorf^a, Lukas Ketter^{a,c}, Emmanuelle Suard^f, Marvin A. Kraft^{a,d}, Brian E. Francisco^g, Michael Ryan Hansen^{*b,c} and Wolfgang G. Zeier^{*a,d}

^a*Institute of Inorganic and Analytical Chemistry, University of Münster, Corrensstraße 28/30, 48149 Münster, Germany.*

^b*Institute of Physical Chemistry, University of Münster, Corrensstraße 28/30, 48149 Münster, Germany.*

^c*International Graduate School BACCARA, Wilhelm-Schickard-Straße 8, 48149 Münster, Germany.*

^d*Institute of Energy Materials and Devices (IMD), IMD 4: Helmholtz-Institut Münster Ionics in Energy Storage, Forschungszentrum Jülich GmbH, 48149 Münster, Germany.*

^e*Bavarian Center for Battery Technology (BayBatt), University of Bayreuth, Universitätsstrasse 30, 95447 Bayreuth, Germany.*

^f*Institut Laue-Langevin, BP 156, 38042 Grenoble Cedex 9, France.*

^g*Solid Power Inc, 486 S Pierce Ave Ste E, Louisville, Colorado, 80027, United States.*

E-mail addresses of corresponding authors:

[*wzeier@uni-muenster.de](mailto:wzeier@uni-muenster.de)

[*mhansen@uni-muenster.de](mailto:mhansen@uni-muenster.de)

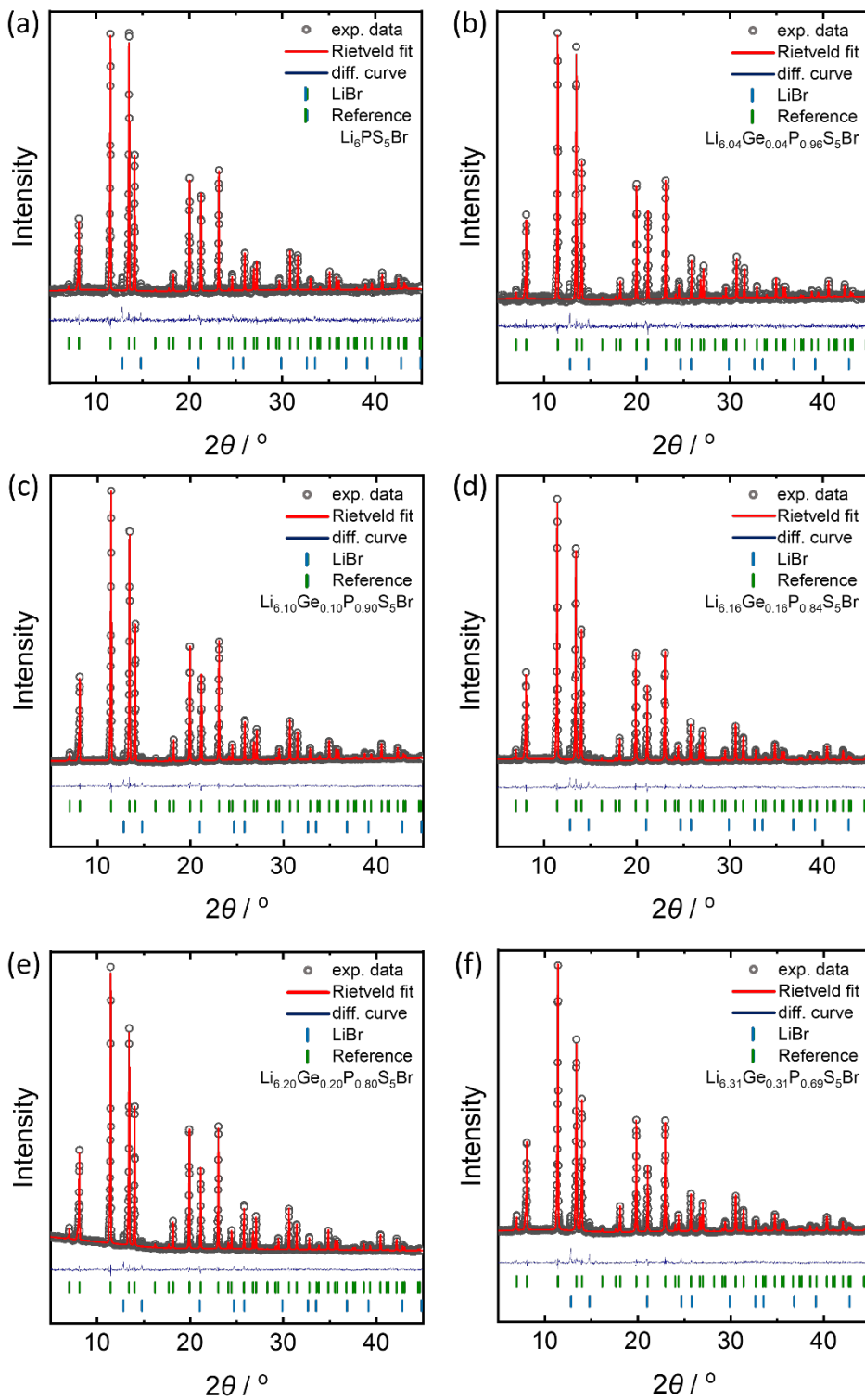


Figure S1. X-ray powder diffraction data and the corresponding Rietveld refinement of the substituted $\text{Li}_{6+x}\text{Ge}_x\text{P}_{1-x}\text{S}_5\text{Br}$. The gray circles represent the experimental data and the red line shows the calculated pattern. The dark blue line denotes the difference profile. The green vertical lines denote the Bragg reflection position from the reference pattern, while the blue vertical lines denote the Bragg reflection position from the side phase of LiBr.

The following tables S1 – S6 include all the crystallographic information extracted Rietveld refinements against X-ray diffraction data. The composition in the following tables for the $Li_{6+x}Ge_xP_{1-x}S_5Br$ substitution series corresponds to the x_{refined} content.

Table S1: Crystallographic data of Li_6PS_5Br obtained from Mo-X-Ray diffraction data. Statistical standard deviations of the refined parameters are shown in parentheses.

$a = 9.9844(2)$ Å, Space group: $F\bar{4}3m$	$\lambda_{\text{Mo-K}\alpha 1} = 0.7093$ Å					
1.6(1) wt.% LiBr						
$R_{\text{wp}} = 2.65\%$, GoF = 1.03						
Atom	Wyckoff site	x	y	z	Occupancy	B_{eq}
LiT5	48h	0.3071	0.0251	0.6929	0.4407	3
LiT5a	24g	0.25	0.017	0.75	0.1186	3
Br1	4a	0	0	1	0.780(5)	3.0(1)
Br2	4d	0.25	0.25	0.75	0.120(5)	1.9(2)
P1	4b	0	0	0.5	1	1.6(1)
S1	4d	0.25	0.25	0.75	0.780(5)	1.9(2)
S2	16e	0.1195(2)	-0.1195(2)	0.6195(2)	1	2.28(7)
S3	4a	0	0	1	0.120(5)	3.0(1)

Table S2: Crystallographic data of $Li_{6.04}Ge_{0.04}P_{0.96}S_5Br$ obtained from Mo-X-Ray diffraction data. Statistical standard deviations of the refined parameters are shown in parentheses.

$a = 10.0188(2)$ Å, Space group: $F\bar{4}3m$	$\lambda_{\text{Mo-K}\alpha 1} = 0.7093$ Å					
1.5(1) wt.% LiBr						
$R_{\text{wp}} = 2.51\%$; GoF = 0.92						
Atom	Wyckoff site	x	y	z	Occupancy	B_{eq}
LiT5	48h	0.3071	0.0251	0.6929	0.4407	3
LiT5a	24g	0.25	0.017	0.75	0.1186	3
Br1	4a	0	0	1	0.899(8)	4.2(1)
Br2	4d	0.25	0.25	0.75	0.101(8)	1.4(2)
P1	4b	0	0	0.5	0.957(8)	0.85(7)
Ge1	4b	0	0	0.5	0.043(8)	0.85(7)
S1	4d	0.25	0.25	0.75	1.3(1)	1.4(2)
S2	16e	0.1190(2)	-0.1190(2)	0.6190(2)	1	2.23(8)
S3	4a	0	0	1	0.101(8)	4.2(1)

Table S3: Crystallographic data of $Li_{6.10}Ge_{0.10}P_{0.90}S_5Br$ obtained from Mo-X-Ray diffraction data. Statistical standard deviations of the refined parameters are shown in parentheses.

$a = 10.0309(8)$ Å, Space group: $F\bar{4}3m$					$\lambda_{Mo-Ka1} = 0.7093$ Å	
0.86(4) wt.% LiBr						
$R_{wp} = 0.98\%$; GoF = 1.19						
Atom	Wyckoff site	x	y	z	Occupancy	B_{eq}
LiT5	48h	0.3071	0.0251	0.6929	0.4407	3
LiT5a	24g	0.25	0.017	0.75	0.1186	3
Br1	4a	0	0	1	0.896(2)	3.65(5)
Br2	4d	0.25	0.25	0.75	0.104(2)	1.66(6)
P1	4b	0	0	0.5	0.896(3)	0.71(6)
Ge1	4b	0	0	0.5	0.104(3)	0.71(6)
S1	4d	0.25	0.25	0.75	0.896(2)	1.66(6)
S2	16e	0.1190(1)	-0.1190(1)	0.6190(1)	1	2.15(3)
S3	4a	0	0	1	0.104(2)	3.65(5)

Table S4: Crystallographic data of $Li_{6.16}Ge_{0.16}P_{0.84}S_5Br$ obtained from Mo-X-Ray diffraction data. Statistical standard deviations of the refined parameters are shown in parentheses.

$a = 10.0531(2)$ Å, Space group: $F\bar{4}3m$					$\lambda_{Mo-Ka1} = 0.7093$ Å	
1.12(5) wt.% LiBr						
$R_{wp} = 1.03\%$; GoF = 1.23						
Atom	Wyckoff site	x	y	z	Occupancy	B_{eq}
LiT5	48h	0.3071	0.0251	0.6929	0.4407	3
LiT5a	24g	0.25	0.017	0.75	0.1186	3
Br1	4a	0	0	1	0.897(2)	3.80(6)
Br2	4d	0.25	0.25	0.75	0.103(2)	1.85(7)
P1	4b	0	0	0.5	0.843(3)	0.75(6)
Ge1	4b	0	0	0.5	0.157(3)	0.75(6)
S1	4d	0.25	0.25	0.75	0.897(2)	1.85(7)
S2	16e	0.1193(1)	-0.1193(1)	0.6193(1)	1	2.12(3)
S3	4a	0	0	1	0.103(2)	3.80(6)

Table S5: Crystallographic data of $\text{Li}_{6.20}\text{Ge}_{0.20}\text{P}_{0.80}\text{S}_5\text{Br}$ obtained from Mo-X-Ray diffraction data. Statistical standard deviations of the refined parameters are shown in parentheses.

$a = 10.0567(1)$ Å, Space group: $F\bar{4}3m$						$\lambda_{\text{Mo-Ka1}} = 0.7093$ Å
0.95(5) wt.% LiBr						
$R_{\text{wp}} = 1.12\%$; GoF = 1.02						
Atom	Wyckoff site	x	y	z	Occupancy	B_{eq}
LiT5	48h	0.3071	0.0251	0.6929	0.4407	3
LiT5a	24g	0.25	0.017	0.75	0.1186	3
Br1	4a	0	0	1	0.904(3)	4.12(6)
Br2	4d	0.25	0.25	0.75	0.096(3)	1.85(8)
P1	4b	0	0	0.5	0.795(4)	0.95(6)
Ge1	4b	0	0	0.5	0.205(4)	0.95(6)
S1	4d	0.25	0.25	0.75	0.904(3)	1.85(8)
S2	16e	0.1198(1)	-0.1198(1)	0.6198(1)	1	2.38(4)
S3	4a	0	0	1	0.096(3)	4.12(6)

Table S6: Crystallographic data of $\text{Li}_{6.31}\text{Ge}_{0.31}\text{P}_{0.69}\text{S}_5\text{Br}$ obtained from Mo-X-Ray diffraction data. Statistical standard deviations of the refined parameters are shown in parentheses.

$a = 10.0811(1)$ Å, Space group: $F\bar{4}3m$						$\lambda_{\text{Mo-Ka1}} = 0.7093$ Å
1.65(6) wt.% LiBr						
$R_{\text{wp}} = 1.01\%$; GoF = 1.21						
Atom	Wyckoff site	x	y	z	Occupancy	B_{eq}
LiT5	48h	0.3071	0.0251	0.6929	0.4407	3
LiT5a	24g	0.25	0.017	0.75	0.1186	3
Br1	4a	0	0	1	0.898(3)	3.90(6)
Br2	4d	0.25	0.25	0.75	0.102(3)	1.80(8)
P1	4b	0	0	0.5	0.693(4)	0.96(6)
Ge1	4b	0	0	0.5	0.307(4)	0.96(6)
S1	4d	0.25	0.25	0.75	0.898(3)	1.80(8)
S2	16e	0.1203(1)	-0.1203(1)	0.6203(1)	1	1.89(4)
S3	4a	0	0	1	0.102(3)	3.90(6)

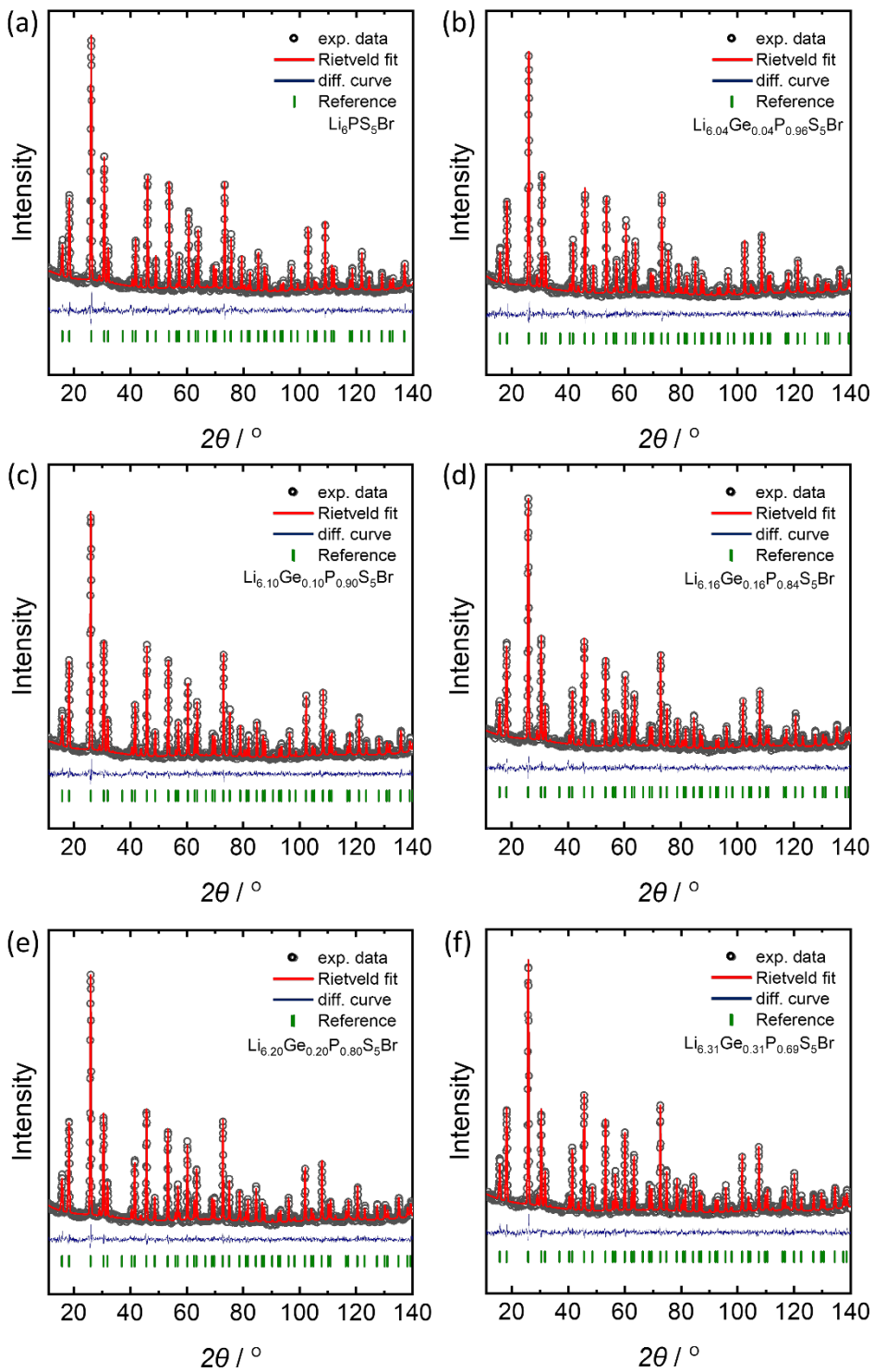


Figure S2. Neutron powder diffraction data and the corresponding Rietveld refinement of the substituted $\text{Li}_{6+x}\text{Ge}_x\text{P}_{1-x}\text{S}_5\text{Br}$. The gray circles represent the experimental data and the red line shows the calculated pattern. The blue line denotes the difference profile. The green vertical lines denote the Bragg reflection position from the reference pattern.

The following tables S7 – S12 include all the crystallographic information extracted Rietveld refinements against neutron powder diffraction data. The composition in the following tables for the $\text{Li}_{6+x}\text{Ge}_x\text{P}_{1-x}\text{S}_5\text{Br}$ substitution series corresponds to the x_{refined} content.

Table S7: Crystallographic data of $\text{Li}_6\text{PS}_5\text{Br}$ obtained from neutron powder diffraction data. Statistical standard deviations of the refined parameters are shown in parentheses.

$a = 9.9845(2)$ Å, Space group: $F\bar{4}3m$						$\lambda_{\text{neutron}} = 1.59289(1)$ Å
1.54(9) wt.% LiBr						
$R_{\text{wp}} = 3.38\%$, GoF = 0.37; weighted Durbin-Watson = 1.06						
Atom	Wyckoff site	x	y	z	Occupancy	B_{eq}
LiT5	48h	0.3098(7)	0.0270(2)	0.6902(2)	0.397(4)	3.8(2)
LiT5a	24g	0.25	0.0270(8)	0.75	0.206(8)	3.8(2)
Br1	4a	0	0	1	0.80(8)	2.9(7)
Br2	4d	0.25	0.25	0.75	0.20(8)	1.87(8)
P1	4b	0	0	0.5	1	1.36(5)
S1	4d	0.25	0.25	0.75	0.80(8)	1.87(8)
S2	16e	0.1188(2)	-0.1188(2)	0.6188(2)	1	2.12(6)
S3	4a	0	0	1	0.20(8)	2.9(7)

Table S8: Crystallographic data of $\text{Li}_{6.04}\text{Ge}_{0.04}\text{P}_{0.96}\text{S}_5\text{Br}$ obtained from neutron powder diffraction data. Statistical standard deviations of the refined parameters are shown in parentheses.

$a = 10.0188(2)$ Å, Space group: $F\bar{4}3m$					$\lambda_{\text{neutron}} = 1.59345(3)$ Å	
0.67(7) wt.% LiBr						
$R_{\text{wp}} = 3.27\%$; GoF = 0.36; weighted Durbin-Watson = 1.21						
Atom	Wyckoff site	x	y	z	Occupancy	B_{eq}
LiT5	48h	0.3082(8)	0.0233(9)	0.6918(8)	0.371(4)	3.5(2)
LiT5a	24g	0.25	0.020(4)	0.75	0.203(7)	3.5(2)
LiT2	48h	0.295(8)	0.093(8)	0.593(8)	0.031(5)	3.5(2)
Br1	4a	0	0	1	0.849(8)	3.27(7)
Br2	4d	0.25	0.25	0.75	0.151(8)	1.76(8)
P1	4b	0	0	0.5	0.957(8)	1.18(5)
Ge1	4b	0	0	0.5	0.043(8)	1.18(5)
S1	4d	0.25	0.25	0.75	0.849(8)	1.76(8)
S2	16e	0.1191(3)	-0.1191(3)	0.6191(3)	1	2.28(6)
S3	4a	0	0	1	0.151(8)	3.27(7)

Table S9: Crystallographic data of $\text{Li}_{6.10}\text{Ge}_{0.10}\text{P}_{0.90}\text{S}_5\text{Br}$ obtained from neutron powder diffraction data. Statistical standard deviations of the refined parameters are shown in parentheses.

$a = 10.0310(1)$ Å, Space group: $F\bar{4}3m$					$\lambda_{\text{neutron}} = 1.59365(2)$ Å	
0.24(5) wt.% LiBr						
$R_{\text{wp}} = 3.28\%$; GoF = 0.36; weighted Durbin-Watson = 1.22						
Atom	Wyckoff site	x	y	z	Occupancy	B_{eq}
LiT5	48h	0.3045(6)	0.0238(8)	0.6955(6)	0.362(5)	3.1(2)
LiT5a	24g	0.25	0.020(4)	0.75	0.198(6)	3.1(2)
LiT2	48h	0.292(5)	0.085(4)	0.585(4)	0.048(4)	3.1(2)
Br1	4a	0	0	1	0.864(8)	3.10(6)
Br2	4d	0.25	0.25	0.75	0.136(8)	1.77(8)
P1	4b	0	0	0.5	0.896(3)	1.17(5)
Ge1	4b	0	0	0.5	0.104(3)	1.17(5)
S1	4d	0.25	0.25	0.75	0.864(8)	1.77(8)
S2	16e	0.1195(3)	-0.1195(3)	0.6195(3)	1	2.08(6)
S3	4a	0	0	1	0.136(8)	3.10(6)

Table S10: Crystallographic data of $\text{Li}_{6.16}\text{Ge}_{0.16}\text{P}_{0.84}\text{S}_5\text{Br}$ obtained from neutron powder diffraction data. Statistical standard deviations of the refined parameters are shown in parentheses.

$a = 10.0531(2)$ Å, Space group: $F\bar{4}3m$					$\lambda_{\text{neutron}} = 1.59351(3)$ Å	
0.57(6) wt.% LiBr						
$R_{\text{wp}} = 3.15\%$; GoF = 0.35; weighted Durbin-Watson = 1.20						
Atom	Wyckoff site	x	y	z	Occupancy	B_{eq}
LiT5	48h	0.3077(9)	0.026(1)	0.6923(9)	0.335(7)	3.2(2)
LiT5a	24g	0.25	0.015(3)	0.75	0.251(7)	3.2(2)
LiT2	48h	0.283(9)	0.069(6)	0.569(6)	0.040(4)	3.2(2)
LiT4	16e	0.15	0.15	0.15	0.041(9)	3.2(2)
Br1	4a	0	0	1	0.886(9)	3.62(7)
Br2	4d	0.25	0.25	0.75	0.114(9)	1.84(9)
P1	4b	0	0	0.5	0.843(3)	1.35(5)
Ge1	4b	0	0	0.5	0.157(3)	1.35(5)
S1	4d	0.25	0.25	0.75	0.886(9)	1.84(9)
S2	16e	0.1201(3)	-0.1201(3)	0.6201(3)	1	2.21(7)
S3	4a	0	0	1	0.114(9)	3.62(7)

Table S11: Crystallographic data of $\text{Li}_{6.20}\text{Ge}_{0.20}\text{P}_{0.80}\text{S}_5\text{Br}$ obtained from neutron powder diffraction data. Statistical standard deviations of the refined parameters are shown in parentheses.

$a = 10.0567(1)$ Å, Space group: $F\bar{4}3m$					$\lambda_{\text{neutron}} = 1.59344(2)$ Å	
0.42(6) wt.% LiBr						
$R_{\text{wp}} = 3.22\%$; GoF = 0.36; weighted Durbin-Watson = 1.20						
Atom	Wyckoff site	x	y	z	Occupancy	B_{eq}
LiT5	48h	0.3042(7)	0.0229(9)	0.6938(7)	0.348(6)	3.1(2)
LiT5a	24g	0.25	0.016(4)	0.75	0.210(6)	3.1(2)
LiT2	48h	0.299(5)	0.075(4)	0.575(4)	0.050 (4)	3.1(2)
LiT4	16e	0.15	0.15	0.15	0.043(6)	3.1(2)
Br1	4a	0	0	1	0.877(8)	3.53(7)
Br2	4d	0.25	0.25	0.75	0.123(8)	1.84(8)
P1	4b	0	0	0.5	0.795(4)	1.21(5)
Ge1	4b	0	0	0.5	0.205(4)	1.21(5)
S1	4d	0.25	0.25	0.75	0.877(8)	1.84(8)
S2	16e	0.1200(3)	-0.1200(3)	0.6200(3)	1	2.19(7)
S3	4a	0	0	1	0.123(8)	3.53(7)

Table S12: Crystallographic data of $\text{Li}_{6.31}\text{Ge}_{0.31}\text{P}_{0.69}\text{S}_5\text{Br}$ obtained from neutron powder diffraction data. Statistical standard deviations of the refined parameters are shown in parentheses.

$a = 10.0811(1)$ Å, Space group: $F\bar{4}3m$	$\lambda_{\text{neutron}} = 1.59346(3)$ Å					
0.59(6) wt.% LiBr						
$R_{\text{wp}} = 3.10\%$; GoF = 0.34; weighted Durbin-Watson = 1.25						
Atom	Wyckoff site	x	y	z	Occupancy	B_{eq}
LiT5	48h	0.3053(7)	0.0227(9)	0.6947(7)	0.333(6)	3.0(2)
LiT5a	24g	0.25	0.014(4)	0.75	0.224(6)	3.0(2)
LiT2	48h	0.303(6)	0.080(4)	0.580(4)	0.055(4)	3.0(2)
LiT4	16e	0.15	0.15	0.15	0.078(7)	3.0(2)
Br1	4a	0	0	1	0.874(8)	3.66(7)
Br2	4d	0.25	0.25	0.75	0.126(8)	1.81(9)
P1	4b	0	0	0.5	0.693(4)	1.12(5)
Ge1	4b	0	0	0.5	0.307(4)	1.12(5)
S1	4d	0.25	0.25	0.75	0.874(8)	1.81(9)
S2	16e	0.1202(3)	-0.1202(3)	0.6202(3)	1	2.02(7)
S3	4a	0	0	1	0.126(8)	3.66(7)

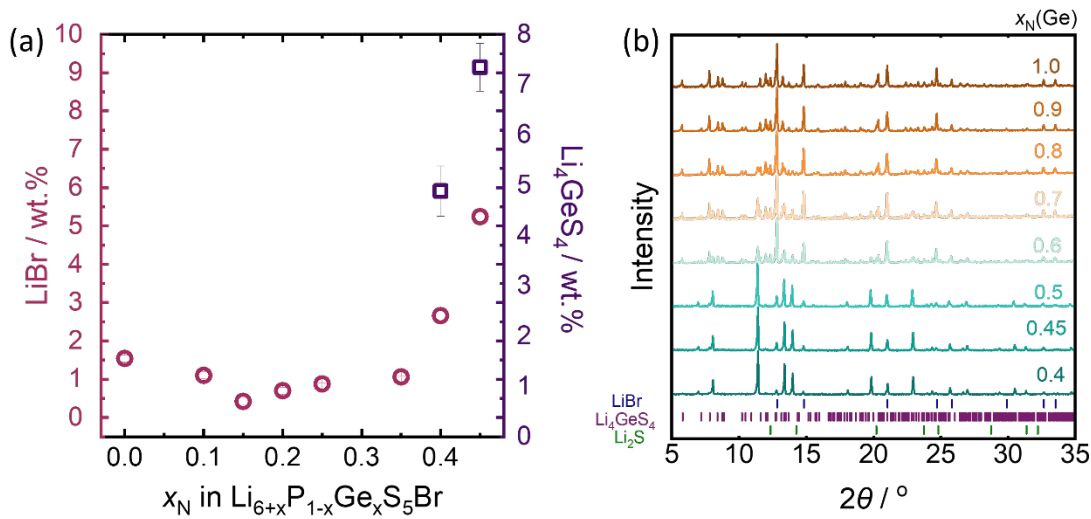


Figure S3. X-ray diffraction data of $\text{Li}_{6+x}\text{Ge}_x\text{P}_{1-x}\text{S}_5\text{Br}$ up to $x_N=1$. (a) The amount of side phases from $x_N(\text{Ge}) = 0$ to $x_N(\text{Ge}) = 0.35$ reveals the successful substitution of Ge(IV) into the argyrodite structure. (b) X-ray diffraction patterns for $x_N(\text{Ge}) > 0.4$ reveal the onset of LiBr, Li_2S and Li_4GeS_4 side phases in the $\text{Li}_6\text{PS}_5\text{Br}$ structure. All patterns correspond to materials annealed at 550 °C for 2h, followed by natural cooling.

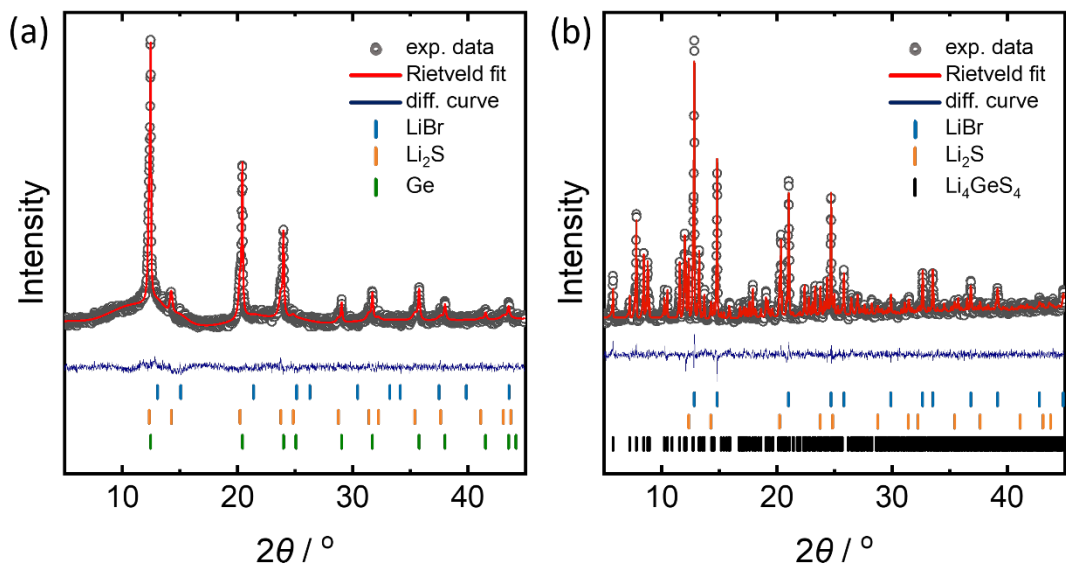


Figure S4. X-ray diffraction patterns of $\text{Li}_7\text{GeS}_5\text{Br}$. (a) $\text{Li}_7\text{GeS}_5\text{Br}$ after ball milling revealing some crystallite content, which cannot be refined or assigned to the argyrodite structure. It consists of 67(2) wt.% Li_2S , 21(1) wt.% Ge and 12(3) wt.% LiBr . (b) $\text{Li}_7\text{GeS}_5\text{Br}$ after 550 °C for 2h, consisting of 64.2(4) wt.% Li_4GeS_4 , 22.5(3) wt.% LiBr and 13.3(4) wt.% Li_2S .

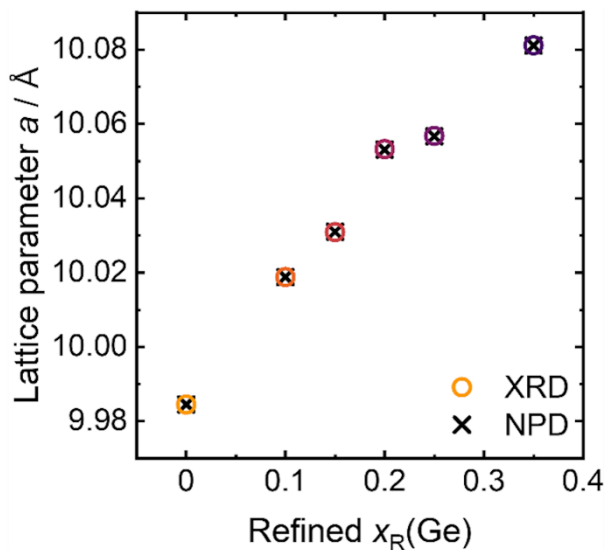


Figure S5. Lattice parameters from XRD and NPD vs. refined $x(\text{Ge})$. Lattice parameters obtained from Rietveld refinements against X-ray diffraction data (open-colored circles) and neutron powder diffraction data (black crosses) demonstrate good agreement between the two refinement methods, confirming the reliability of the structural analysis.

Nuclear Magnetic Resonance Analysis

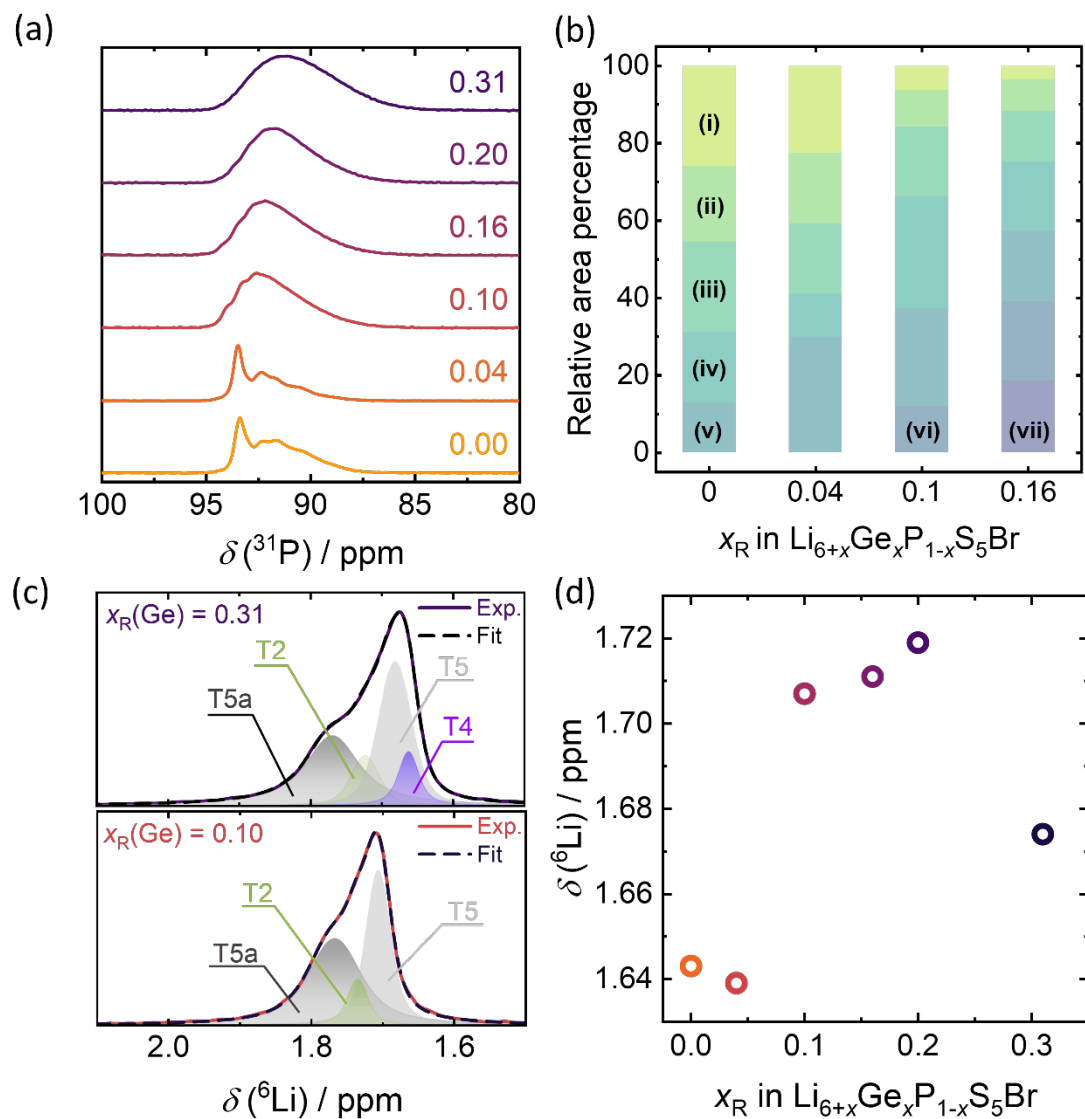


Figure S6. Solid-state ^{31}P and ^6Li MAS NMR for the substitution series of $\text{Li}_{6+x}\text{Ge}_x\text{P}_{1-x}\text{S}_5\text{Br}$. (a) Stacked ^{31}P MAS NMR spectra of the $\text{Li}_{6+x}\text{Ge}_x\text{P}_{1-x}\text{S}_5\text{Br}$ substitution series recorded at spinning frequency of 25.0 kHz. (b) Relative contribution (area integral) of the different ^{31}P resonance signals to the total fit. Higher number (vii,vi,...) indicates resonances at lower ppm. (c) Tentative deconvolution of the ^6Li MAS NMR spectra of $x_{\text{R}}(\text{Ge}) = 0.10$ and $x_{\text{R}}(\text{Ge}) = 0.31$. (d) Trend in chemical shift of the highest intensity ^6Li resonance.

Modified Bloembergen-Purcell-Pound (BPP) model for ${}^7\text{Li}$ spin-lattice (T_1) relaxometry.

For Li-argyrodites, the shape of the ${}^7\text{Li}$ T_1 -relaxation curve has been described using a modified BPP model as follows:

$$\frac{1}{T_1} = C \left(\frac{\tau_c}{1 + (\omega_0 \tau_c)^{1+\beta}} + \frac{4\tau_c}{1 + (2\omega_0 \tau_c)^{1+\beta}} \right), 0 < \beta \leq 1 \dots\dots (1)$$

$$\tau_c = \tau_0 \exp\left(\frac{E_{a,HT}}{k_B T}\right) \dots\dots (2)$$

$$\beta = \frac{E_{a,LT}}{E_{a,HT}} \dots\dots (3)$$

Where:

T_1 = spin-lattice relaxation constant

C = a prefactor indicating the strength of dipolar and quadrupolar interactions leading to relaxation

τ_c = motional correlation time

ω_0 = angular Larmor frequency of ${}^7\text{Li}$ at the given magnetic field strength

β = a correction factor (asymmetry parameter) to the original BPP formula (developed for isotropic diffusion in liquids) which considers the deviation from ideality ($\beta = 1$) in solids due to different reasons like structural disorder, dimensionality of the jump processes etc.

$E_{a,HT}$ = activation energy obtained from the high-temperature flank of the rate curve

$E_{a,LT}$ = activation energy obtained from the low-temperature flank of the rate curve

The asymmetry parameter β reflects the difference in the activation barriers of the motional processes that dominates the high- and low-temperature flank of the rate curve, thus accounting for the asymmetric nature of the rate curves in solid ion conductors. A more detailed discussion on the modified BPP formula can be found in the article by Wankmiller *et al.*¹

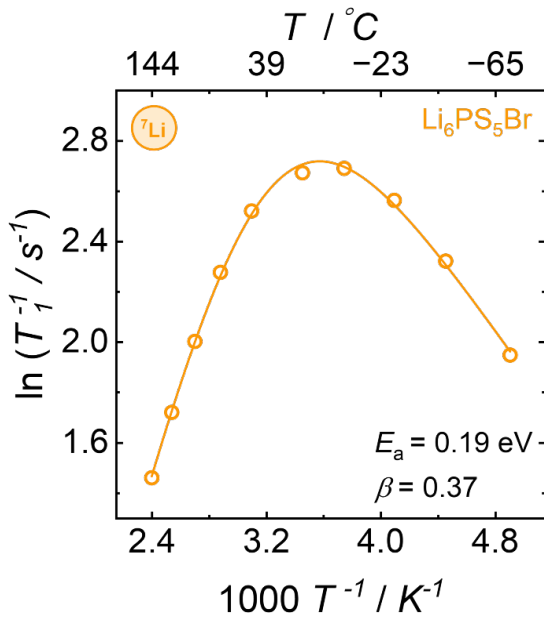


Figure S7. ${}^7\text{Li}$ spin-lattice (T_1) relaxation data for $\text{Li}_6\text{PS}_5\text{Br}$. Arrhenius plot of the data with a modified-BPP fit ($E_{a,HT} = 0.19 \text{ eV}$, $\beta = 0.37$).

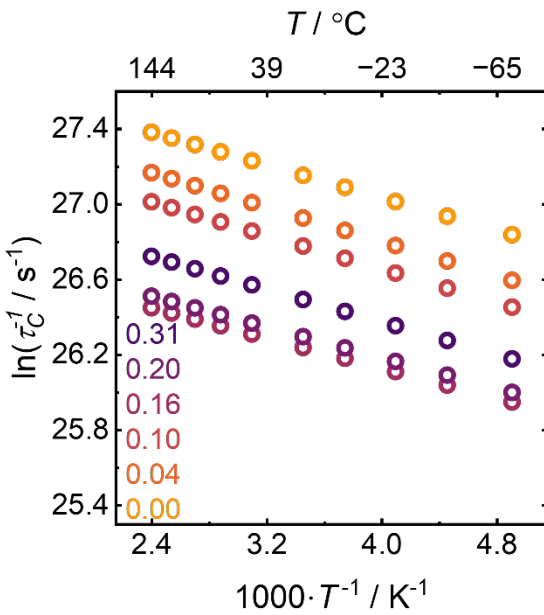


Figure S8. Arrhenius plot of the motional correlation rates ($1/\tau_c$). The trend in the motional correlation rates (calculated using $E_{a,HT}$ and $\tau_{c,0}$ obtained from the modified BPP fits) at different temperatures seems to follow the Br-/S²⁻site disorder and the T2-T2 distance.

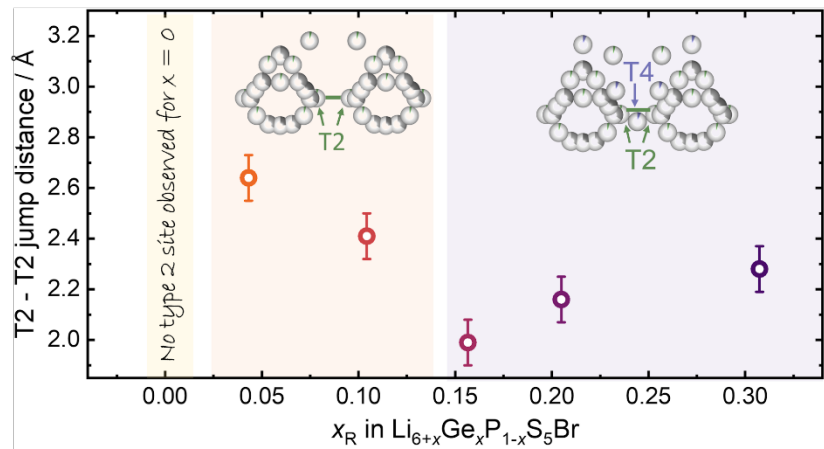


Figure S9. T2-T2 jump distance. The trend in T2-T2 jump distance with increasing Ge(IV) content obtained from Rietveld refinements.

Table S13: Different parameters obtained from modified BPP fits of the ${}^7\text{Li}$ T_1 -relaxation data for the samples with different $x_{\text{R}}(\text{Ge})$. $E_{\text{a}, \text{HT}}$ and $E_{\text{a}, \text{LT}}$ were obtained from high- and low-temperature flank of the modified-BPP fits, respectively. The asymmetry parameter β reflects the difference between the abovementioned two activation energies.

$x_{\text{R}}(\text{Ge})$	$E_{\text{a}, \text{HT}}$ / eV	$E_{\text{a}, \text{LT}}$ / eV	β	C / s^{-2}	T_{max} / K	R_{max} / s^{-1}	$1/\tau_c$ at 300 K / s^{-1}
0.00	0.187	0.069	0.37	6.78×10^9	280	15.13	1.81×10^{12}
0.04	0.197	0.052	0.26	6.52×10^9	288	15.75	1.43×10^{12}
0.10	0.192	0.059	0.31	7.03×10^9	294	16.38	1.24×10^{12}
0.16	0.172	0.064	0.37	7.72×10^9	294	17.25	7.43×10^{11}
0.20	0.176	0.063	0.36	7.94×10^9	296	17.87	7.81×10^{11}
0.31	0.187	0.074	0.39	9.16×10^9	308	20.19	9.37×10^{11}

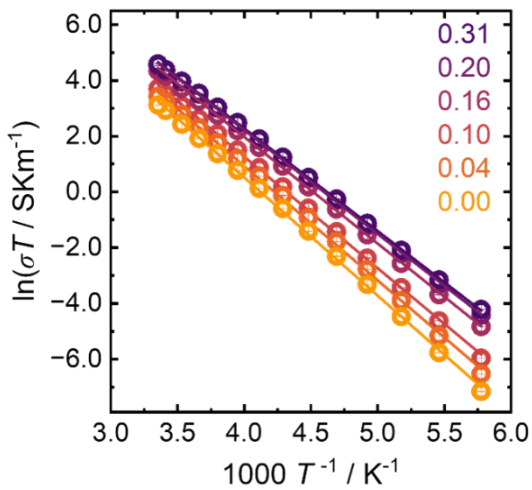


Figure S10. T-dependent PEIS. Representative Arrhenius plots of the temperature-dependent ionic conductivity measurements, measured in a range from $-100\text{ }^\circ\text{C}$ to $25\text{ }^\circ\text{C}$ for the $\text{Li}_{6+x}\text{Ge}_x\text{P}_{1-x}\text{S}_5\text{Br}$ substitution series.

Half-Cell testing

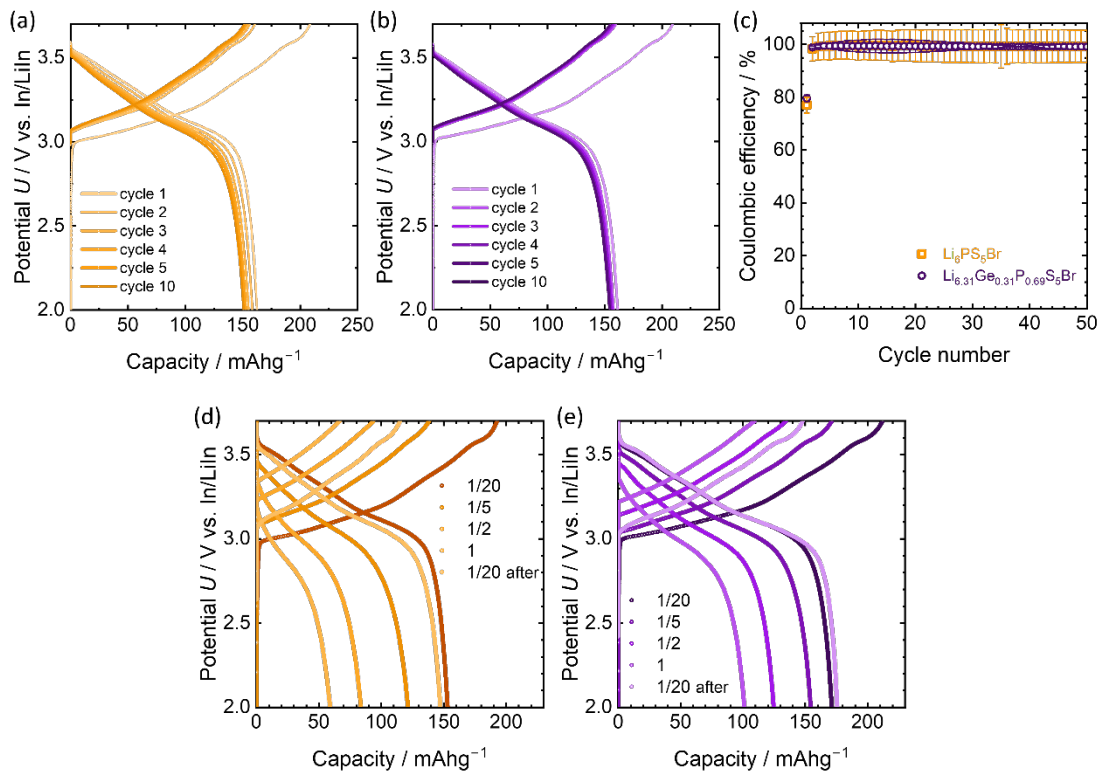


Figure S11. Charge-discharge profiles and Coulomb efficiency. No additional processes are observed for the first ten cycles of NCM-83 based half-cells with (a) $\text{Li}_6\text{PS}_5\text{Br}$ and (b) $\text{Li}_{6.31}\text{Ge}_{0.31}\text{P}_{0.69}\text{S}_5\text{Br}$ as solid electrolytes. (c) Development of the Coulomb efficiency for half-

cells with either $\text{Li}_6\text{PS}_5\text{Br}$ or $\text{Li}_{6.31}\text{Ge}_{0.31}\text{P}_{0.69}\text{S}_5\text{Br}$ as solid electrolyte. (d, e) Comparison of the first charge and discharge profiles at each C-rate during the rate tests reveal that no additional processes occur at higher cycling currents in half cells with (d) $\text{Li}_6\text{PS}_5\text{Br}$ and (e) $\text{Li}_{6.31}\text{Ge}_{0.31}\text{P}_{0.69}\text{S}_5\text{Br}$ as solid electrolytes.

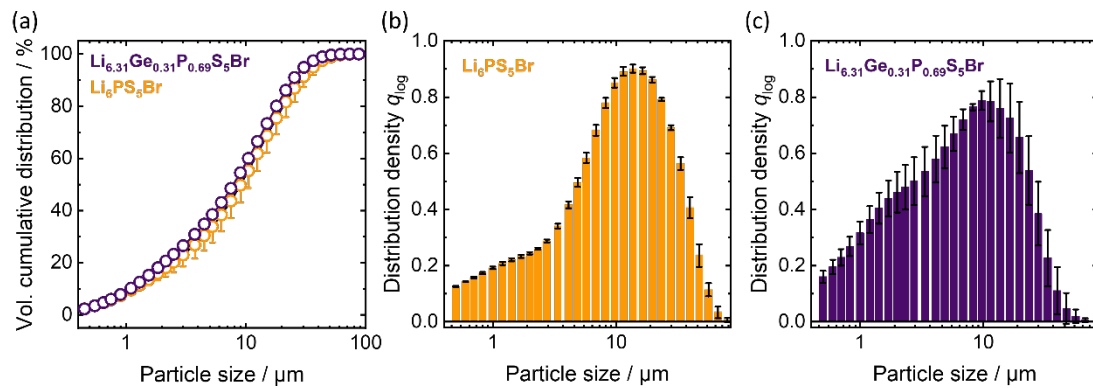


Figure S12. Particle size distribution of $\text{Li}_6\text{PS}_5\text{Br}$ and $\text{Li}_{6.31}\text{Ge}_{0.31}\text{P}_{0.69}\text{S}_5\text{Br}$. (a) The volumetric cumulative distribution for both solid electrolytes shows that both solid electrolytes have similar particle size distributions within uncertainty, as calculated from triplicate measurements. The respective distribution density histograms of (b) $\text{Li}_6\text{PS}_5\text{Br}$ and (c) $\text{Li}_{6.31}\text{Ge}_{0.31}\text{P}_{0.69}\text{S}_5\text{Br}$ show that $\text{Li}_6\text{PS}_5\text{Br}$ contains slightly less agglomerates of smaller particle size and some larger agglomerates, as represented by the $D_{10} = 1.3 \mu\text{m}$, $D_{50} = 10.1 \mu\text{m}$ and $D_{90} = 30.1 \mu\text{m}$, compared to the respective values of $D_{10} = 1.1 \mu\text{m}$, $D_{50} = 8.1 \mu\text{m}$ and $D_{90} = 25.0 \mu\text{m}$. The y-axis is plotted in logarithmic scale to emphasize that the differences are within experimental uncertainty.

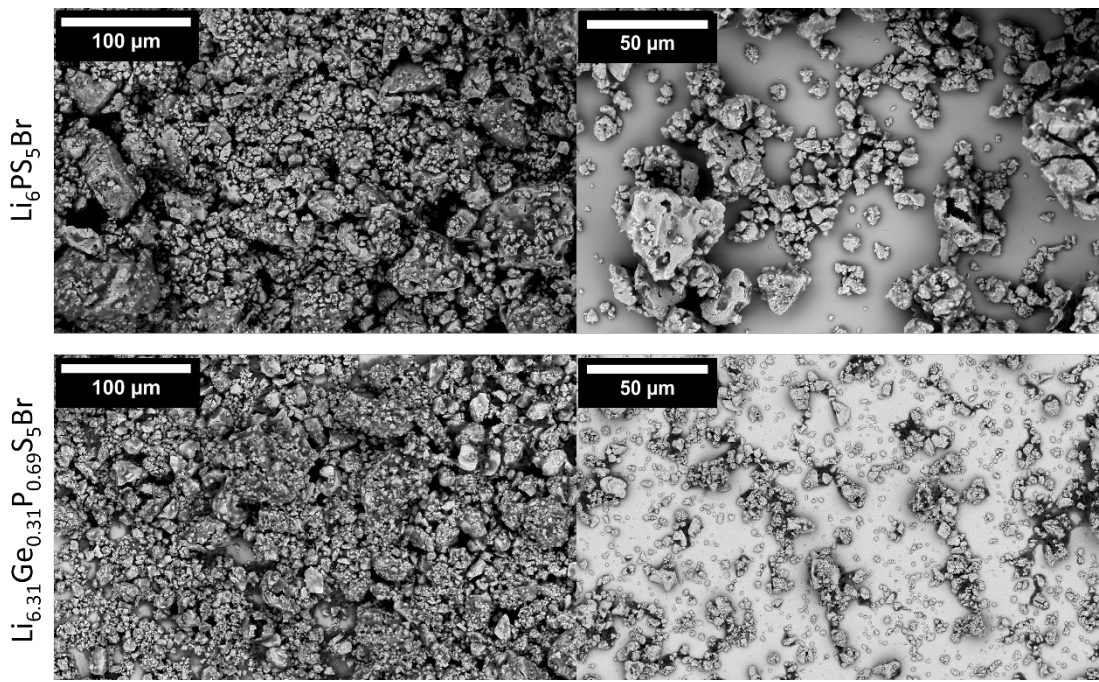


Figure S13. Scanning electron microscopy images of $\text{Li}_6\text{PS}_5\text{Br}$ (top) and $\text{Li}_{6.31}\text{Ge}_{0.31}\text{P}_{0.69}\text{S}_5\text{Br}$ (below) in two different magnifications. The SEM images show no significant differences between the investigated materials.

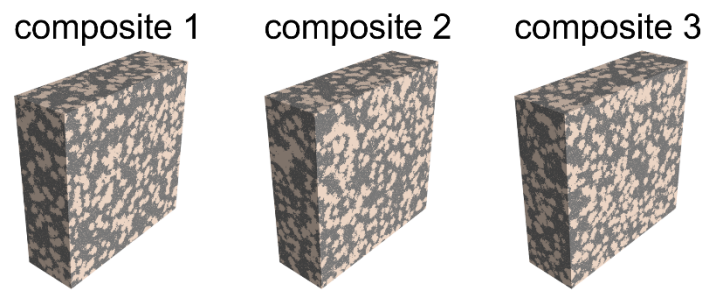


Figure S14. Virtual microstructures. The voxel representation of 3 composite structures as used as structural input in the resistor network model, consisting of a 46:54 volume fraction of NCM-83:SE. Three composite structures were used in analogy to the experimental triplicate measurements, in order to evaluate the uncertainties of the effective ionic conductivities.

Table 14: Resistor network model. The values of electronic and ionic conductivity used for the solid electrolytes and NCM-83 as input parameters. The effective ionic conductivity (σ_{eff}) corresponds to the effective conductivities of the virtual composites as extracted from the model as output parameters.

Input		Output			Mean effective conductivity
$\sigma_{\text{NCM}} / \text{mS}\cdot\text{cm}^{-1}$	$\sigma_{\text{SE}} / \text{mS}\cdot\text{cm}^{-1}$	$\sigma_{\text{comp1}} / \text{mS}\cdot\text{cm}^{-1}$	$\sigma_{\text{comp2}} / \text{mS}\cdot\text{cm}^{-1}$	$\sigma_{\text{comp3}} / \text{mS}\cdot\text{cm}^{-1}$	$\sigma_{\text{eff}} / \text{mS}\cdot\text{cm}^{-1}$
5.22	10^{-100}	0.937	0.902	0.939	0.92 ± 0.02
10^{-100}	3.8	0.450	0.439	0.441	0.443 ± 0.006
10^{-100}	0.8	0.095	0.092	0.093	0.093 ± 0.002

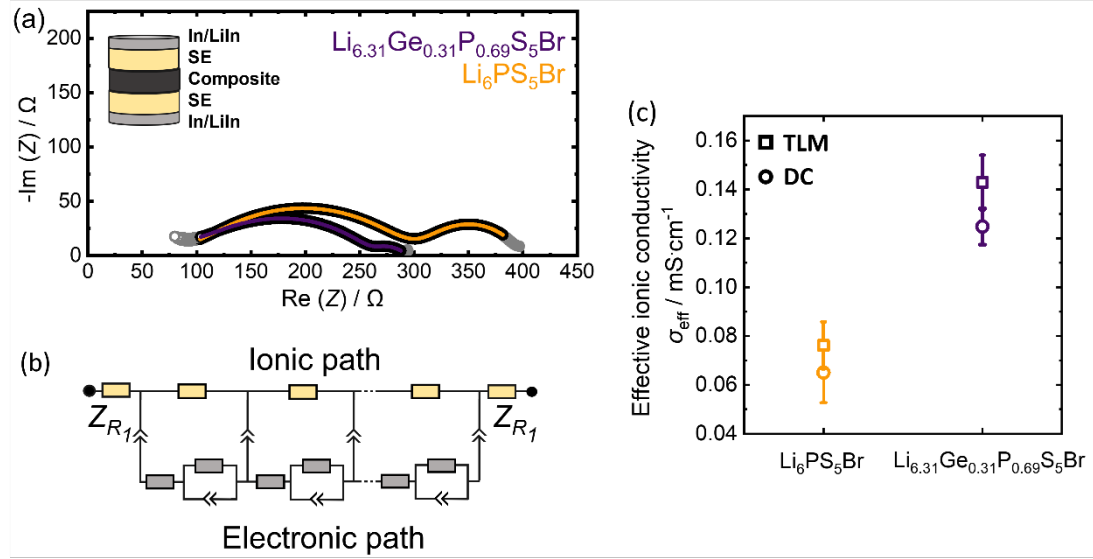


Figure S15. Partial ionic transport in the composite. (a) Nyquist plots show the lower resistance of $\text{Li}_{6.31}\text{Ge}_{0.31}\text{P}_{0.69}\text{S}_{5}\text{Br}$ vs. $\text{Li}_6\text{PS}_5\text{Br}$. (b) A schematic representation of the T-type transmission line model used to fit the impedance data. (c) Comparison of the effective ionic conductivity values as obtained from (i) fitting the T-type transmission line model against impedance data, (ii) DC polarization measurements. The effective conductivity of $\text{Li}_{6.31}\text{Ge}_{0.31}\text{P}_{0.69}\text{S}_{5}\text{Br}$ in the composite is higher than $\text{Li}_6\text{PS}_5\text{Br}$, confirming the indication that the enhanced performance of $\text{Li}_{6.31}\text{Ge}_{0.31}\text{P}_{0.69}\text{S}_{5}\text{Br}$ is attributed to its enhanced transport properties compared to $\text{Li}_6\text{PS}_5\text{Br}$.

REFERENCES

- (1) Wankmiller, B.; Hansen, M. R. Observation of Li^+ Jumps in Solid Inorganic Electrolytes over a Broad Dynamical Range: A Case Study of the Lithium Phosphidosilicates Li_8SiP_4 and $\text{Li}_{14}\text{SiP}_6$. *J. Magn. Reson. Open* **2023**, 14–15, 100098. <https://doi.org/10.1016/j.jmro.2023.100098>.